Journal of Alloys and Compounds 509 (2011) 2588–2596

Contents lists available at ScienceDirect

Journal of Alloys and Compounds

journal homepage: www.elsevier.com/locate/jallcom

Fabrication of mesh-like bismuth oxide single crystalline nanoflakes and their visible light photocatalytic activity

Rui Chen, Zhu-Rui Shen, Hu Wang, Hui-Jing Zhou, Yu-Ping Liu, Da-Tong Ding, Tie-Hong Chen*

Institute of New Catalytic Materials Science, Key Laboratory of Energy-Material Chemistry and Engineering Research Center of Energy Storage & Conversion (MOE), College of Chemistry, Nankai University, Weijin Road 94, Tianjin 300071, PR China

ARTICLE INFO

Article history:
Received 22 July 2010
Received in revised form
11 November 2010
Accepted 15 November 2010
Available online 23 November 2010

Keywords:
Bismuth oxide
Bismuth oxalate
Precursor
Lysine
Morphology
Photocatalytic activity

ABSTRACT

Mesh-like bismuth oxide single crystalline nanoflakes were synthesized via a bismuth oxalate precursor way. During the synthesis procedure bismuth oxalate precipitate was hydrothermally treated, and variation of the pH value of synthesis solution as well as the addition of L-lysine could effectively tune the crystal phase and morphology of the bismuth oxalate precursor. Depending on the crystalline phase of the precursors and the calcination temperature, monoclinic α-Bi_2O_3 and tetragonal β-Bi_2O_3 were selectively obtained. Optical properties of the Bi_2O_3 materials were investigated by UV–vis absorption and the results proved that bismuth oxides were visible light responsive. Photodegradation of rhodamine B was used as a model reaction to test the photocatalytic activity of the Bi_2O_3 samples. The photocatalytic activity of bismuth oxides was related to its crystalline phase and morphology.

1. Introduction

The morphology and microstructure control of materials have attracted growing interests, because materials with novel functionalities depend not only on the composition, but also on the morphology. Catalysts differing in their crystal faces, edges and defects show obvious difference in catalytic activity [1]. The photocatalytic activity of semiconductor oxides was also found to be strongly affected by the crystal size, morphology and microstructure. For example, Testino et al. demonstrated that a substantial improvement of the photocatalytic activity of TiO_2 could be achieved by a careful design of the particle morphology [2]. Unfortunately, as a photocatalyst titania works only under UV-light irradiation, development of visible light induced photocatalyst is still a challenge [3–8]. Bismuth-based visible light induced photocatalysts have been reported, such as Bi_2WO_4 [9,10], $BiVO_4$ [11–13], $CaBi_2O_4$ [14], and $Bi_5FeTi_3O_{15}$ [15]. These new bismuth-based materials show great potential in better utilization of solar energy for visible light induced photocatalysis.

Bismuth oxides exhibit excellent properties, such as high refractive index [16], high dielectric permittivity [17], as well as marked photoluminescence property [18]. Therefore, they have been widely used in many fields such as gas sensors, solid oxide fuel cells, optical coating, and ceramic glass manufacturing. Bismuth oxides have also been proved to be good photocatalyst in water splitting and decontamination under visible light irradiation [19]. Recently, bismuth oxides with various morphologies were synthesized by either physical or chemical methods. Li et al. reported a template-synthesis of Bi–Bi_2O_3 core–shell nanotubes by oxidizing Bi nanowire in AAM (anodic alumina membrane) [20]. Bismuth oxide nanowires together with Bi droplets were synthesized by an oxidative metal vapor transport deposition technique [21]. δ-Bi_2O_3 rods accompanied by a trace amount of α-Bi_2O_3 were successfully prepared by means of halide chemical vapor deposition using BiI_3 and O_2 as starting material [22]. Zhou et al. fabricated δ-Bi_2O_3 hierarchical nanostructures assembled by nanosheets through a template-free aqueous method [23]. α-Bi_2O_3 nanoparticles have been produced by femtosecond laser ablation in ethanol at room temperature [24]. However, it is still a challenge to selectively fabricate pure bismuth oxide in specific crystalline phase through a facile soft-chemical way.

The use of metal salts precursor for the synthesis of metal oxide has been well developed as early as 1980s and this method was successfully used to fabricate nanocrystalline metal oxides by simple thermal decomposition of precursor salts or compounds. The resultant oxide powders generally showed very fine crystallite size and aggregated to form mesopores or nanopores [25–31]. Recently, our group has developed an amino acid modified oxalate precursor way

* Corresponding author. Fax: +86 22 2350 7975.
E-mail address: chenth@nankai.edu.cn (T.-H. Chen).

0925-8388/$ – see front matter © 2010 Elsevier B.V. All rights reserved.
doi:10.1016/j.jallcom.2010.11.102

Table 1
Synthesis parameters and the morphology of bismuth oxalate precursors and Bi_2O_3.

Precursor	Additive	Synthesis pH	Bi_2O_3 after calcination	Morphology
S1	6 mmol lysine	8.4	C1-α[a]	Mesh-like nanoflakes
S2	1 mmol lysine	8.4	C2-α[a]	Submicron plates
S3	None	1.1	C3-α[a]	Submicron rods
			C3-β[b]	Submicron rods
S4	None	2.4	Not calcined	Mixed submicron rods and plates
S5	None	4.4	Not calcined	Mixed submicron rods and plates
S6	None	8.4	C6-α[a]	Submicron plates
S7	1 mmol lysine	1.1	C7-β[b]	Submicron particles
S8	6 mmol lysine	1.1	C8-β[b]	Submicron particles

[a] The bismuth oxalate precursor was calcined at 350 °C for 8 h, and α-Bi_2O_3 was obtained.
[b] The bismuth oxalate precursor was calcined at 270 °C for 5 h, and β-Bi_2O_3 was obtained.

to fabricate mesoporous CeO_2, Mn_2O_3, and MnO_2 with hierarchical nanoarchitecture [22–34]. The effect of amino acids on the formation of hierarchical structure of mesoporous CeO_2 and MnO_2 was examined. Glutamate ions were used to control the morphology of hydroxyapatite [35]. Lu et al. reported highly ordered snowflake-like structures of bismuth sulfide nanorods prepared with the aid of glutathione [36].

In the present study, we report a facile hydrothermal synthetic route for the synthesis of bismuth oxide nanostructures with bismuth oxalate as precursors followed by calcination. By changing pH of the synthesis solution or adding L-lysine as crystal growth modifier, controllable synthesis of bismuth oxalate with different morphologies was achieved. Subsequently, mesh-like nanoflakes, submicron plates and submicron rods of monoclinic α-Bi_2O_3 and particles and submicron rods of tetragonal β-Bi_2O_3 were selectively obtained by adjusting decomposition temperature. In addition, the photocatalytic performances of these Bi_2O_3 nanostructures exhibited a morphology-dependent activity on degradation of rhodamine B (RhB) under visible light irradiation.

2. Experimental

2.1. Synthesis

All the reagents were of analytical grade and were used as received without further purification. In a typical synthesis, 1.920 g $Bi(NO_3)_3{\cdot}5H_2O$ (4 mmol) and 1.760 g L-lysine (12 mmol) were dissolved in 20 mL deionized water. Then, 20 mL 0.15 M $Na_2C_2O_4$ solution was added. After continuous stirring for 30 min, the resulted suspension solution was put into a 50 mL stainless steel autoclave and kept at 160 °C for 24 h. Then the product (bismuth oxalate precursor) was collected by filtration, washed with deionized water and ethanol, dried at 60 °C for 12 h. α-Bi_2O_3 was obtained by thermal decomposition of the bismuth oxalate precursor in air at 350 °C after 8 h.

With or without the addition of L-lysine, synthesis was also performed similar to the process described above but under different pH value, adjusted by an aqueous nitric acid solution (1.0 M) or sodium hydroxide solution (2.0 M), respectively. Those obtained bismuth oxalate precursors were denoted as S1–S8 (described in Table 1). β-Bi_2O_3 was obtained by thermal decomposition of bismuth oxalate precursors in air at 270 °C for 5 h. The corresponding calcined products of bismuth oxides were named as C1–C8 (Table 1).

2.2. Characterization

The powder X-ray diffraction (XRD) patterns were measured on Bruker D8 Focus using CuK_α ($\lambda = 0.1541$ nm) radiation. The thermogravimetry and differential thermal analysis (TG-DTA) were performed on a Rigaku TG-DTA thermal analyzer at a linear heating rate of 20 °C/min, and α-Al_2O_3 was used as a reference. Scanning electron microscopy (SEM) was measured on Shimadzu SS-550 scanning electron microscope. Transmission electron microscopy (TEM), high-resolution transmission electron microscopy (HRTEM), and selected-area electron diffraction (SAED) characterizations were carried out on a Philips Tecnai F20 instrument working at 200 kV. UV–vis diffuse reflectance spectrums (DRS) were measured by using a Shimadu UV-2450 UV-vis spectrophotometer using an integrating sphere accessory. X-ray photoelectron spectroscopy (XPS) measurements were taken with a Kratos Axis Ultra DLD spectrometer.

2.3. Measurement of the photocatalytic activity

The photocatalytic decolorization of 10^{-5} mol/L RhB dye solution was measured in a XPA-7 photocatalytic reactor (made in Xujiang Electromechanical Plant, Nanjing, China) equipped with a 500 W Xe lamp as the irradiation source. For our photocatalytic reactor, 10 quartz tubes were put in a rotating frame so that they could be exposed to light for the same intensity of illumination. By this way we could measure the photocatalytic activity of 10 samples at one time and the data were more reliable than those measured individually. A 420 nm cutoff filter was used to completely remove all wavelengths shorter than 420 nm to ensure irradiation only with visible-light. In each experiment, 0.010 g of catalysts was separately added into 10 mL RhB solution in a quartz tube. Firstly, the catalysts were uniformly distributed by 5 min ultrasonic dispersion. In order to establish adsorption–desorption equilibrium between the dye and catalyst, the suspension was stirred in the dark for thirty minutes. At irradiation time intervals of 1 h, 0.5 mL solutions were collected, diluted to 1.5 mL by deionized water, and then centrifuged (8000 rpm, 5 min) to remove the photocatalyst particles. The solution was analyzed by a 721Z UV–vis spectrophotometer and the absorbance at 552 nm was monitored. All the experiments were performed at ambient condition.

3. Results and discussion

3.1. Structure and morphology of the mesh-like bismuth oxide

As described in Section 2, bismuth oxide was successfully synthesized through a simple L-lysine modified oxalate precursor way. The XRD pattern of the precursor powder collected after hydrothermal treatment (Fig. 1a) showed sharp and intensive diffraction peaks indicating high crystallinity of the product. The diffraction peaks could not be indexed to any known structure and may be indexed to a new or mixed phases of bismuth oxalate.

Low-magnification SEM image in Fig. 2a showed that the as-synthesized sample was mainly composed of nanoflakes. Fig. 2b shows that most of the nanoflakes were approximately 100 nm in thickness and the nanoflakes randomly accumulated together. Thermogravimetry analysis and differential thermal analysis were

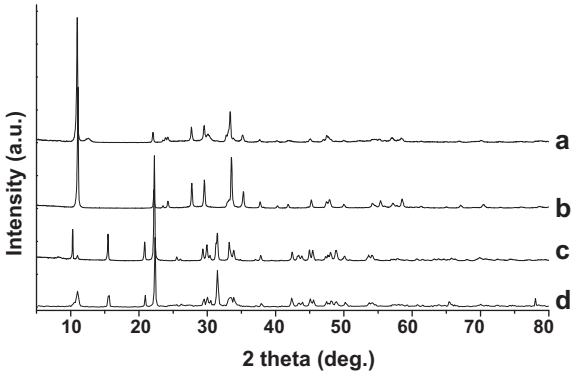

Fig. 1. XRD pattern of the as-synthesized bismuth oxalate with the assistance of L-lysine at different pH value: (a) sample S1 (pH 8.4, 6 mmol L-lysine), (b) S2 (pH 8.4, 1 mmol L-lysine), (c) S7 (pH 1.1, 1 mmol L-lysine) and (d) S8 (pH 1.1, 6 mmol L-lysine).

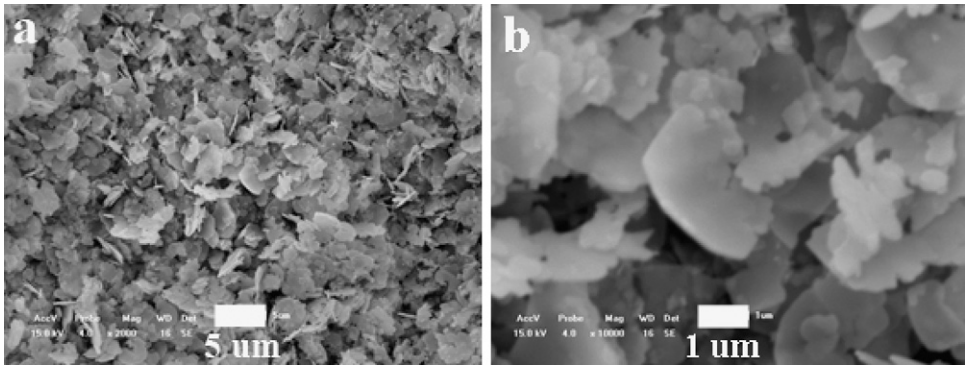

Fig. 2. SEM images of the as-obtained bismuth oxalate precursor (sample S1).

employed in order to investigate the decomposition behavior with increasing temperature. Bismuth oxide generally has four polymorphic forms like α-, β-, γ-, and δ-Bi_2O_3 in monoclinic, tetragonal, body-centered and cubic structure, respectively. Among those phases, two stable polymorphic forms with the transition temperature $\alpha \rightarrow \delta$ at 730 °C and the other two metastable phases were identified depending on the cooling procedures [37]. TG-DTA curve of the as-synthesized bismuth oxalate nanoflakes was shown in Fig. 3. The weight loss at 20–352 °C was due to the transformation from precursor to bismuth oxide. TGA study showed one endothermic peak at 352 °C and two exothermic peaks at 379 °C and 740 °C. The first one was due to the decomposition of bismuth oxalate, the second one could be attributed to a trace amount of phase transformation of Bi_2O_3 from some metastable phase to α-Bi_2O_3, and the third one could be attributed to a transformation of a low temperature stable phase to a high temperature stable phase. Because of the high speed of temperature increase during the measurement (20 °C/min), the decomposition of precursor would not be completed at 352 °C within a short time. Complete decomposition could be achieved by a continuous calcination in muffle oven as long as 8 h. TG-DTA curve of the sample after calcination at 350 °C for 8 h (Fig. 3 inset) showed that there was no weight loss during 20–800 °C. It is convinced that in order to obtain α-Bi_2O_3, the calcination temperature of bismuth oxalate precursors could be set to 350 °C.

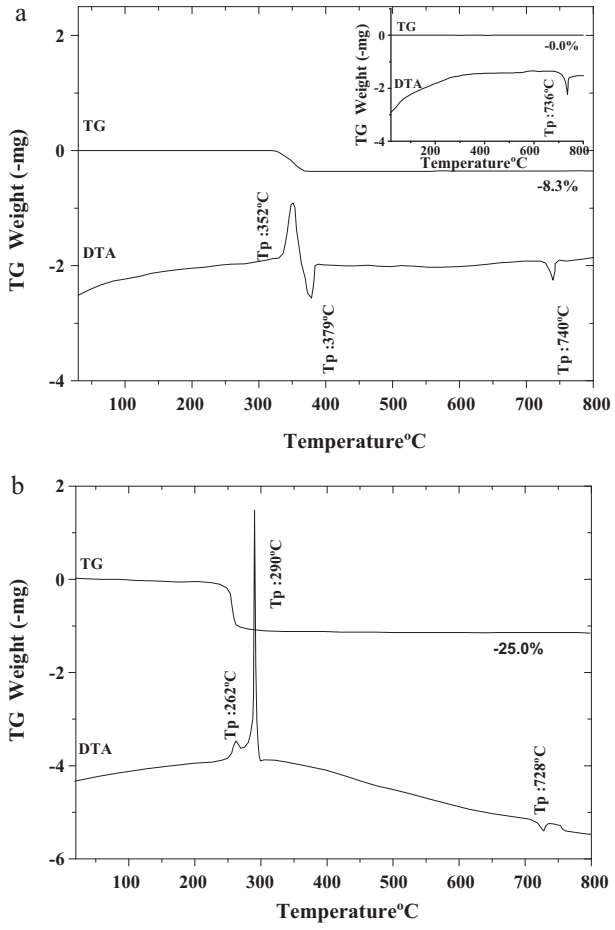

Fig. 3. TG-DTA curves of the as-obtained bismuth oxalate precursor (sample S1). TG-DTA curves of bismuth oxalate precursors (sample S3).

The TEM image of a typical individual nanoflake (Fig. 4c) further confirmed the mesh-like morphology with the pore diameter about 40–200 nm. The sharp diffraction spots shown in the selected-area electron diffraction pattern proved that the mesh-like Bi_2O_3 nanoflake was single crystalline. The lattice fringe spacing of 0.33 nm was in good agreement with the values of (1 2 0) or (−1 2 1) lattice planes of monoclinic Bi_2O_3.

The Bi 4f XPS spectra were acquired to determine chemical state of Bi species. As shown in Fig. 5, the wide and symmetric peak suggested the existence of Bi^{3+}, and there was no sign of Bi^{5+}. The XPS spectra demonstrated that Bi species in the mesh-like nanoflake C1-α were present in the form of Bi_2O_3, corresponding to the binding energy (BE) of 158.7 and 164.0 eV in $Bi_{4f7/2}$ and $Bi_{4f5/2}$ levels, respectively [38]. As a kind of ionic crystal, Bi peaks of the bismuth oxalate precursor S1 appeared at a higher binding energy, ca. 159.0 and 164.3 eV.

3.2. Influence of the synthetic parameters

Mitchell and Guzman reported a coral-like CeO_2 mesostructure obtained through cerium oxalate decomposition method and concluded that the morphology was only dependent on the synthesis pH value whereas the influence of amino acids was neglected [39]. Actually, our previous work demonstrated that the different state of the ionization equilibrium of amino acid at different pH values could effectively control the crystal growth behavior [40]. It is well known that amino acids have both acidic functional groups (–COOH) and basic functional groups ($–NH_2$), which can not only effectively change the acid–base properties of system, but also exhibit adsorption or coordination properties. To clearly investigate the effect of pH and amino acids during the synthesis procedure, experiments were performed by adjusting pH of solution and adding different amounts of amino acids at a settled pH value, respectively. First, the precursors were synthesized in the absence of L-lysine at different pH values to investigate the pH influence on the crystal phase and morphology of the precursors. Then,

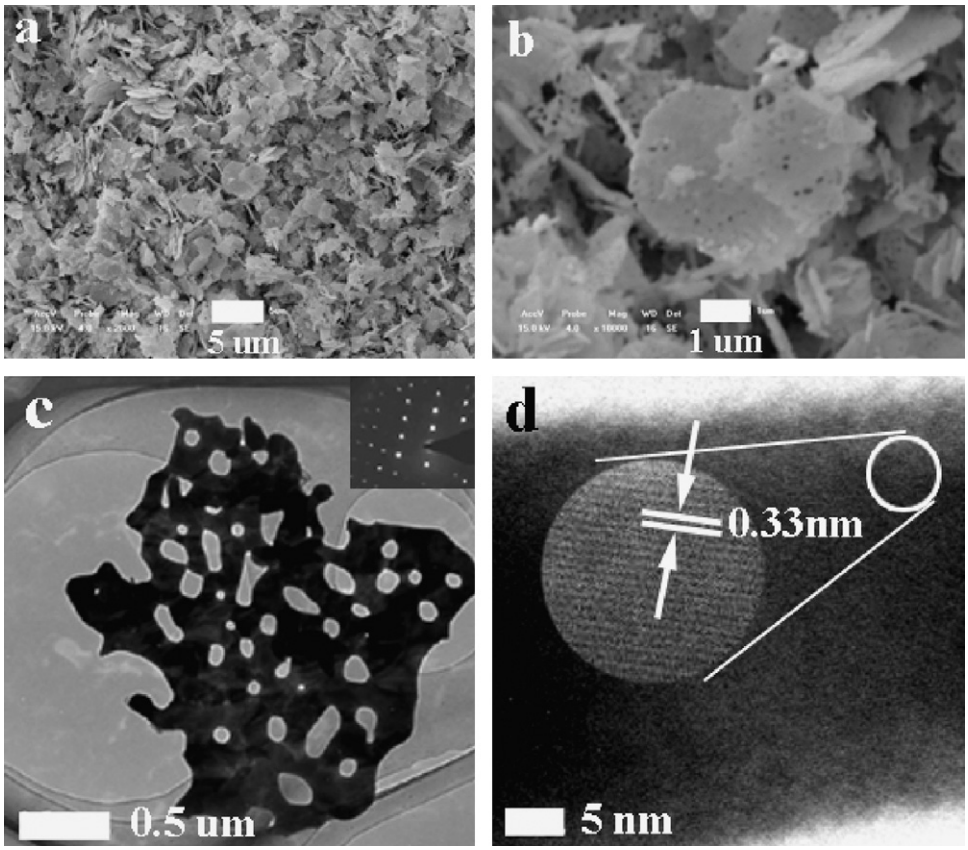

Fig. 4. (a and b) SEM images of mesh-like Bi_2O_3 nanoflakes (sample C1-α), and (c and d) TEM and HRTEM of mesh-like Bi_2O_3 (sample C1-α); the inset in (c) is the corresponding SAED pattern.

different amounts of amino acids were added while keeping the pH at a certain value. Table 1 shows the synthesis parameters and morphology of the precursors and the bismuth oxides in detail.

3.2.1. The effect of pH values (in the absence of L-lysine)

If pH values of synthesis solution were adjusted to 1.1, 2.4, 4.4 and 8.4, samples were denoted as S3, S4, S5 and S6, respectively (Table 1). In order to exclude the formation of $Bi(OH)_3$ and Bi_2O_3 at moderate strong or strong alkali solution, the final pH value was adjusted not higher than 8.4. The XRD patterns of the precursors were shown in Fig. 6. XRD pattern of sample S3 (prepared at pH 1.1) was consistent with a bismuth oxalate ($BiOHC_2O_4$)·$2H_2O$ reported by Monnereau et al. [41]. While the synthesis was performed at pH 8.4, the XRD pattern of the precursor changed greatly (Fig. 6d), which was same as that of sample S1. This indicates that the crystal phase of the precursors was determined by the synthesis pH value, no matter lysine was added or not. However, as shown below, the addition of lysine at certain pH value could modify the morphology of the precursors even if they were of the same crystal phase. The XRD patterns of the precursors synthesized at pH values of 2.4 and 4.4 displayed mixed crystal phases (sample S4 and S5).

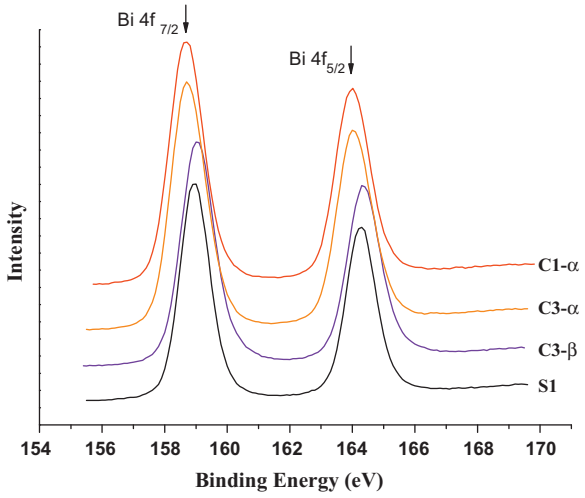

Fig. 5. Bi 4f photoelectron spectra of bismuth oxide samples.

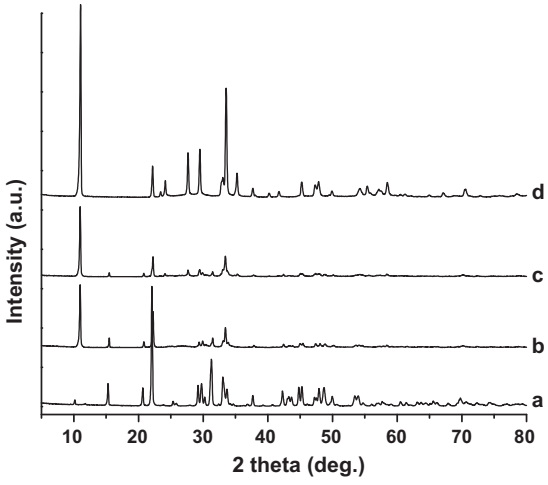

Fig. 6. XRD patterns of bismuth oxalate synthesized at different pH value without the addition of lysine: (a) pH = 1.1 (sample S3), (b) pH = 2.4 (S4), (c) pH = 4.4 (S5) and (d) pH = 8.4 (S6).

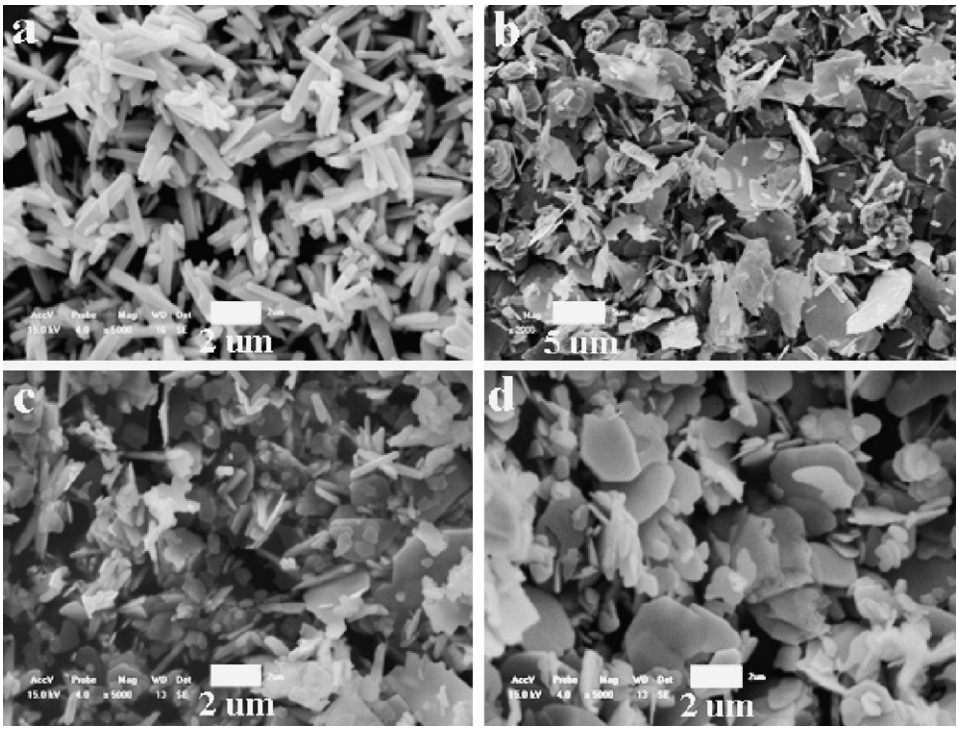

Fig. 7. SEM pictures of bismuth oxalate synthesized at different pH value without the addition of lysine: (a) pH = 1.1 (sample S3), (b) pH = 2.4 (S4), (c) pH = 4.4 (S5) and (d) pH = 8.4 (S6).

The morphology of samples S3, S4, S5 and S6 were shown in Fig. 7. Sample S3 synthesized at pH of 1.1 displayed well dispersed and uniform submicron rods ca. 500 nm in diameter (Fig. 7a). When the pH value was increased to 8.4, morphology of the precursor changed obviously to plate-like structure with a thickness of 300–500 nm (Fig. 7d). The morphologies of sample S4 and S5 displayed mixed submicron rods and plates, in agreement with their XRD patterns of mixed crystal phases. This morphology evolution phenomenon of the precursors synthesized at different pH was consistent with the XRD results which showed a phase transformation of bismuth oxalate at different pH values.

In the TG curve of bismuth oxalate precursor S3 (Fig. 3), there was only one weight loss step at the temperature range of 25–260 °C. The weight loss corresponding to an exothermic peak at 262 °C was attributed to the bismuth oxalate precursor decomposition into Bi_2O_3. The corresponding DTA curve showed other two peaks at 290 °C and 728 °C, and this behavior was similar with that as reported by Rivenet et al. [42], which were ascribed to the β-$Bi_2O_3 \rightarrow \alpha$-$Bi_2O_3$ and α-$Bi_2O_3 \rightarrow \delta$-$Bi_2O_3$ phase transition. For submicron plate-like S6, on account of the same crystal structure as nanoflake-like S1, it showed the same decomposing behavior as nanoflake-like S1 (data not shown). Based on the above discussion, it is implied that bismuth oxides with different crystalline phases could be selectively obtained by adjusting the decomposition temperature of the precursors synthesized at certain pH value.

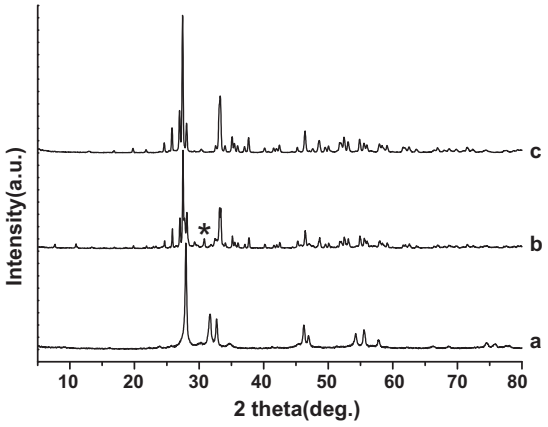

Fig. 8. XRD patterns of samples obtained by decomposing the precursors in air: (a) sample C3-β, (b) C3-α, and (c) C6-α. The little impurities indexed by asterisk was assigned to $Bi_5O_7NO_3$ which is liable to form in moderate acid condition.

The corresponding XRD patterns of the oxides after calcination of S3 and S6 were shown in Fig. 8. For sample C3-β, after calcination in air at 270 °C for 5 h, all diffraction peaks shown in Fig. 8a could be indexed as Bi_2O_3 with a tetragonal structure, in good agreement with JCPDS card No. 65-1209. If sample S3 was calcined in air at 350 °C for 5 h, the XRD peaks of C3-α (Fig. 8b) were in good agreement with JCPDS card No. 71-2274 (monoclinic Bi_2O_3). The decomposition behavior of S6 was same as that of S1 and after calcination at 350 °C for 5 h, the corresponding XRD pattern of C6-α (Fig. 8c) could be well-indexed to a pure monoclinic phase of Bi_2O_3, which was consistent with JCPDS card No. 65-2336. Fig. 9 displays SEM images of the oxides samples, which revealed that the morphologies of bismuth oxides were consistent with their corresponding bismuth oxalate precursors. The Bi 4f XPS spectra of the samples were shown in Fig. 5. The Bi 4f peaks shifted to lower binding energy when the calcination temperature increased, indicating that the average electron density of Bi–O was increased at higher decomposition temperature.

3.2.2. The effect of L*-lysine on morphology of the bismuth oxalate precursors*

The impact of organic molecules on the crystallization of inorganic materials is important. For example, amino acids as a special kind of bimolecular can effectively control the crystal growth process [43–46]. In order to investigate the influence of L-lysine, synthesis of precursors were performed with different amount of L-lysine at certain pH value. Besides the sample S1 (pH 8.4, 6 mmol

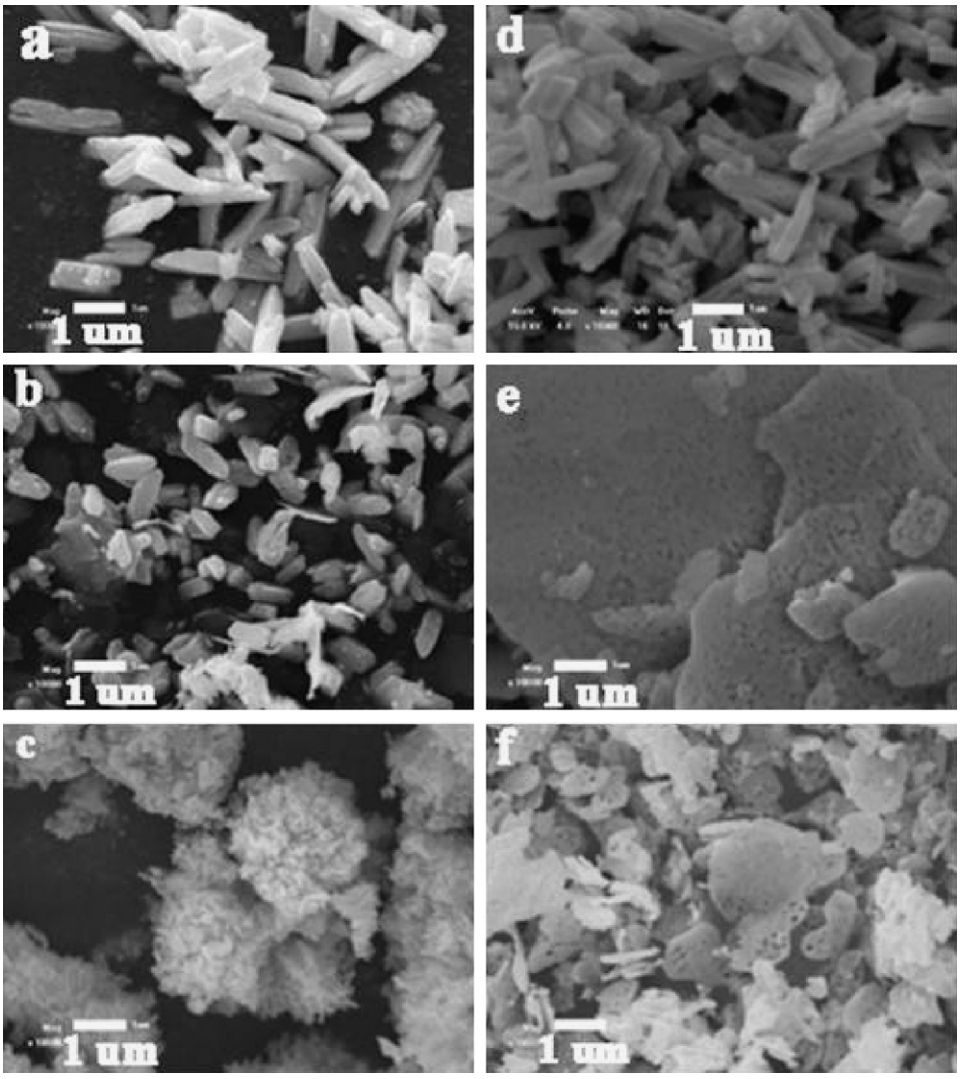

Fig. 9. SEM images of (a) sample C3-β, (b) C7-β, (c) C8-β, (d) C3-α, (e) C6-α and (f) C2-α.

L-lysine), the XRD pattern (Fig. 1b) of sample S2 (pH 8.4, 1 mmol L-lysine) was the same to that of S1 (Fig. 1a). At pH of 1.1, the precursors S7 (with 1 mmol L-lysine) and S8 (with 6 mmol L-lysine) exhibited same XRD pattern, which was similar to that of S3 (synthesized at pH 1.1 but without lysine). This phenomenon implies that if the pH value remained unchanged, crystal forms of the precursors were consistent with each other either with or without L-lysine addition. So L-lysine here was only a crystal growth modifier to control the morphology (see below) and did not influence the crystal phase of the precursors. Fig. 10 reveals that with the addition of L-lysine as the additive, the morphology of the precursors varied greatly, especially for samples synthesized at pH = 1.1. Particles were obtained when the synthesis was performed by adding 1 mmol L-lysine at pH = 1.1 (Fig. 10a and b). Maintaining the pH value at 1.1 but increasing the amounts of L-lysine to 6 mmol, chrysanthemum like structures assembled from nanorods was the main product (Fig. 10c and d). Compared to precursor S3 prepared without addition of L-lysine, the diameter of the rods was reduced to nanoscale (ca. 100 nm) and hierarchical architectures were assembled by the nanorods. If the pH value of solution was adjusted to weak alkaline (pH = 8.4), plates with different thickness were obtained by adding different amounts of L-lysine. In Fig. 10e with the addition of 1 mmol L-lysine, the plate was about 300 nm in thickness; while with the addition of 6 mmol L-lysine, the thickness was ca. 100 nm (Fig. 2b).

As the basic structural units of protein, amino acids contain hydrophilic functional groups like $-NH_2$ or –COOH and have the ability of complex formation with metal ions. In our experimental procedure, by introducing L-lysine and after hydrothermal reaction, the morphology would be changed by selective absorption of L-lysine on a particular crystal face of the bismuth oxalate. It is well known that the surface energies of the specific crystal facets are different from each other. It was presumed that during the hydrothermal treatment L-lysine was selectively absorbed onto a specific surface and inhibited the growth of this surface. As a result, thinner nanoflakes can be obtained after more L-lysine added into the weak alkaline system. The exact interaction between L-lysine molecular and bismuth oxalate precursor deserves further investigation.

The corresponding XRD of the thermally decomposed products from bismuth oxalates synthesized under the control of L-lysine at different pH value were shown in Fig. 11. In Fig. 11c and d, for the products decomposed at 270 °C for 5 h from the precursors synthesized at pH = 1.1, the intensive diffraction peaks corresponding to 28°, 31.8°, 32.7°, 46.2° and 55.6° were indexed to the (2 0 1), (0 0 2), (2 2 0), (2 2 2) and (4 2 1) diffractions of the tetragonal phase (JCPDS

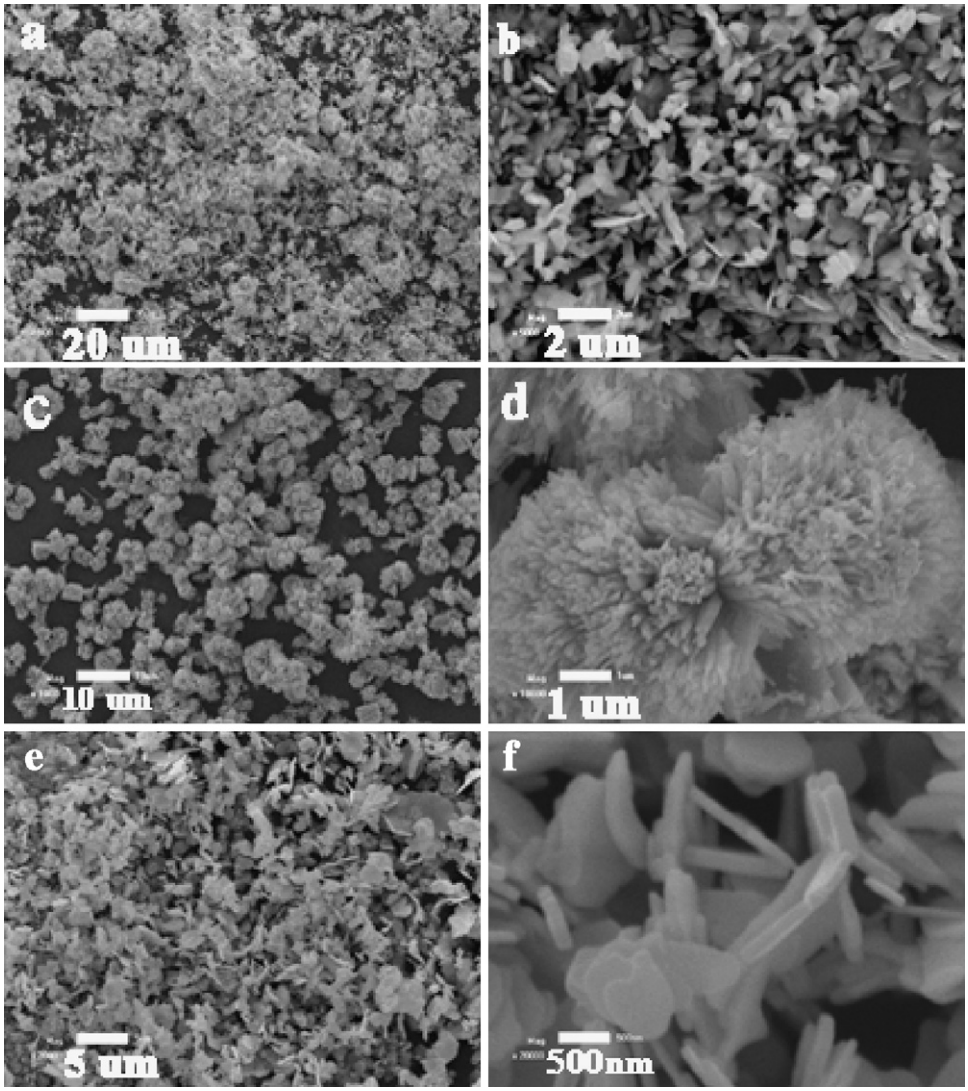

Fig. 10. SEM images of the as-synthesized bismuth oxalate with the assistance of L-lysine at different pH value: (a and b) sample S7 (pH = 1.1 and 1 mmol L-lysine), (c and d) sample S8 (pH = 1.1 and 6 mmol L-lysine), (e and f) sample S2 (pH = 8.4 and 1 mmol L-lysine).

No. 27-50). The obtained products decomposed from the precursors synthesized at pH = 8.4 were indexed to a pure monoclinic phase of Bi_2O_3 (Fig. 11a and b). Fig. 9a–c shows the SEM images of tetragonal β-Bi_2O_3, which revealed that the products decomposed from S3, S7 and S8 preserved the morphology of their precursors. The images of monoclinic α-Bi_2O_3 shown in Fig. 9d–f also displayed uniform rods or plates as their precursors.

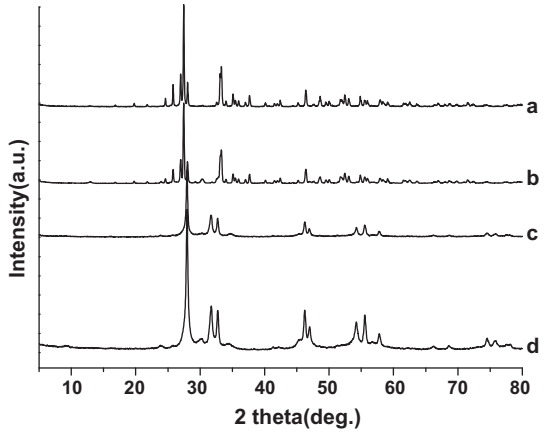

Fig. 11. XRD patterns of the corresponding decomposing products: (a) sample C1-α, (b) C2-α, (c) C7-β and (d) C8-β.

All the above results demonstrated that pH value of the synthesis system played an important role in controlling the crystal phase and morphology of the precursors, and L-lysine could effectively modify the crystal growth behavior and control the morphology of the products. These observations were similar to our early work reported for the crystallization of PbS [40] which demonstrated that both the pH value and amino acid could effectively control the crystal growth under hydrothermal condition.

3.3. Optical and photocatalytic activities of the obtained Bi_2O_3

The electronic structure of the semiconductor plays a crucial role in its photocatalytic activity. For monoclinic Bi_2O_3, the valance band (VB) is formed by a hybridization of Bi 6s and O 2P orbitals, while the conduction band is composed of Bi 6p orbitals [47]. Fig. 12 displays the UV–vis diffuse reflection spectra of tetragonal bismuth oxide and monoclinic bismuth oxide. All optical absorption of the monoclinic samples was nearly the same. As a crystalline semiconductor, the optical absorption near the band edges follows the formula $\alpha h\nu = A(h\nu - E_g)^{n/2}$, where α, ν, E_g and A are the absorp-

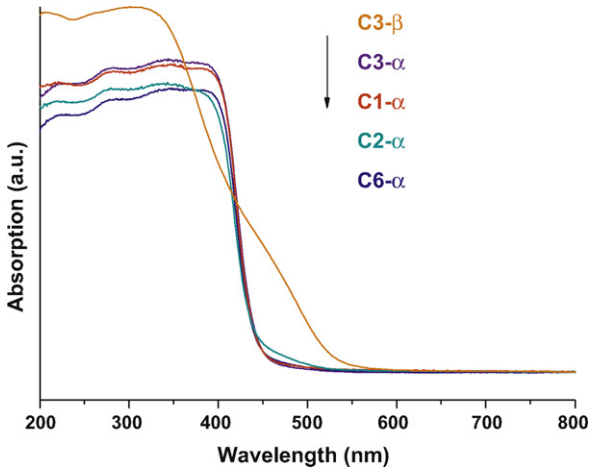

Fig. 12. UV–vis absorption spectra of the Bi_2O_3 samples.

tion coefficient, light frequency, band gap energy and a constant, respectively. Among them, n depends on the characteristics of the transition in a semiconductor and the value of n for Bi_2O_3 was 1 [48]. The band gap energy (E_g value) of Bi_2O_3 could be estimated from a plot of $(\alpha h\nu)^2$ versus photo energy ($h\nu$) [49]. The extrapolated value (the straight lines to the X axis) of $h\nu$ at $\alpha = 0$ gave the absorption edge energy corresponding to $E_g = 2.85$ eV, which is in visible light region. In contrast to the monoclinic phase obtained at 350 °C, the spectra of the tetragonal phase β-Bi_2O_3 obtained at 270 °C (the orange line in Fig. 12) showed a red shift and the absorption edge shifted to a longer wavelength.

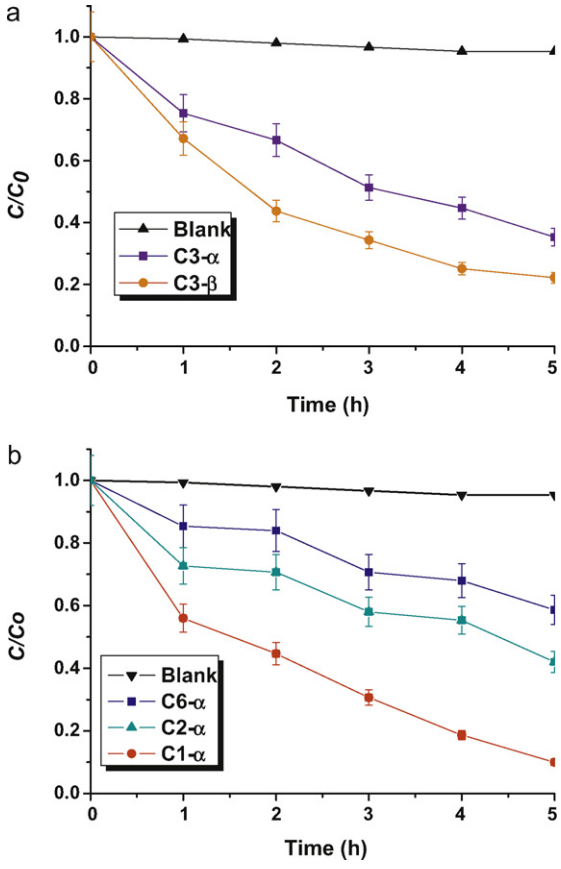

Fig. 13. Photodegradation of RhB in the presence of Bi_2O_3 under visible light irradiation.

Photocatalytic activities of the obtained Bi_2O_3 were evaluated by the degradation of RhB in water under visible light irradiation ($\lambda > 420$ nm). Before the photocatalytic reaction, the RhB solution was first irritated under visible light in the absence of the photocatalyst to examine its stability. After 5 h of irradiation time, the RhB degradation rate was merely 6%. In addition, the concentration of RhB almost did not decrease in dark condition after the Bi_2O_3 and RhB solution reached the adsorption–desorption equilibrium. Therefore, the presence of both catalysts and illumination was necessary for efficient degradation. The removal of RhB using different bismuth oxides as photocatalyst was shown in Fig. 13. Both the tetragonal and monoclinic Bi_2O_3 nanostructures resulted in sharp increase of RhB photodegradation rates, which demonstrated that these Bi_2O_3 materials were active photocatalysts. The influence of crystalline phase on photocatalytic activity is shown in Fig. 13a, the results confirmed that tetragonal β-Bi_2O_3 rods (C3-β) exhibited better activity than monoclinic α-Bi_2O_3 rods (C3-α) due to the smaller band gap. If bismuth oxides were synthesized in the absence of L-lysine, the degradation of RhB in 5 h were 35% for C6-α. Whereas, after adding L-lysine as morphology modifier in synthesis, the degradation of RhB in 5 h was 90% and 58% for nanoflake C1-α and plate-like C2-α, respectively. The plate obtained in the absence of L-lysine (shown in Fig. 7) was approximately 300–500 nm in thickness. However, with the addition of L-lysine and the pH value adjusted to 8.5, either 1 mmol or 6 mmol L-lysine was added, the thickness of the plates obviously became thinner. The thinner plates would provide more active sites and absorb more reactive species in the solution. The high surface-to-volume ratios of the mesh-like nanoflakes could facilitate the diffusion of the reactants and products during the reaction [50]. Our experimental evidences proved that the addition of L-lysine could modify the process to fabricate bismuth oxide materials and enhance their ability of RhB degradation under visible light irradiation.

4. Conclusions

Bismuth oxides were fabricated via a bismuth oxalate precursor method. With the addition of L-lysine as the crystal growth modifier, bismuth oxalate nanoflakes were synthesized. After calcination, mesh-like bismuth oxide single crystalline nanoflakes were obtained. In the synthesis, pH value was an important factor on both the crystal phase and morphology of bismuth oxalate during the hydrothermal treatment. L-Lysine as a crystal growth modifier could effectively control the morphology of bismuth oxalate. Depending on the crystalline phase of the precursors and the calcination temperature, monoclinic α-Bi_2O_3 and tetragonal β-Bi_2O_3 were selectively obtained. Photodegradation of rhodamine B under visible light irradiation was used as a model reaction to test the photocatalytic activity of the Bi_2O_3 samples. The photocatalytic activity of bismuth oxide was related to its crystalline phase and morphology. This work would inspire further research on the morphological control of metal oxides by the organic molecule-controlled precursor way.

Acknowledgments

This work was supported by Natural Science Foundation of China (Grants No. 20873070 and 20973095), National Basic Research Program of China (2009CB623502), NCET of Ministry of Education (NCET-07-0448) and MOE (IRT-0927).

References

[1] M.B.J. Roeffaers, B.F. Sels, H. Uji-i, F.C. De Schryver, P.A. Jacobs, D.E. De Vos, J. Hofkens, Nature 439 (2006) 572.

[2] A. Testino, I.R. Bellobono, V. Buscaglia, C. Canevali, M. D'Arienzo, S. Polizzi, R. Scotti, F. Morazzoni, J. Am. Chem. Soc. 129 (2007) 3564.
[3] R. Asahi, T. Morikawa, T. Ohwaki, K. Aoki, Y. Taga, Science 293 (2001) 269.
[4] K. Nishijima, Y. Fujisawa, N. Murakami, T. Tsubota, T. Ohno, Appl. Catal. B: Environ. 84 (2008) 584.
[5] A.I. Kontos, V. Likodimos, T. Stergiopoulos, D.S. Tsoukleris, P. Falaras, Chem. Mater. 21 (2009) 662.
[6] J.X. Yu, S.W. Liu, Z.L. Xiu, W.N. Yu, G.J. Feng, J. Alloys Compd. 461 (2008) L17.
[7] G. Colón, M. Maicu, M.C. Hidalgo, J.A. Navío, Appl. Catal. B: Environ. 67 (2006) 41.
[8] Y.D. Liu, F. Xin, F.M. Wang, S.X. Luo, X.H. Yin, J. Alloys Compd. 498 (2010) 179.
[9] C. Zhang, Y.F. Zhu, Chem. Mater. 17 (2005) 3537.
[10] Y. Tian, G.M. Hua, W. Xu, N. Li, M. Fang, L.D. Zhang, J. Alloys Compd. (2010), doi:10.1016/j.jallcom.2010.09.010.
[11] A Kudo, K. Omori, H. Kato, J. Am. Chem. Soc. 121 (1999) 11459.
[12] L.Z. Li, B. Yan, J. Alloys Compd. 476 (2009) 624.
[13] Y. Shen, M.L. Huang, Y. Huang, J.M. Lin, J.H. Wu, J. Alloys Compd. 496 (2010) 287.
[14] J.W. Tang, Z.G. Zou, J.H. Ye, Angew. Chem. Int. Ed. 43 (2004) 4463.
[15] S.M. Sun, W.Z. Wang, H.L. Xu, L. Zhou, M. Shang, L. Zhang, J. Phys. Chem. C 112 (2008) 17835.
[16] H.T. Fan, X.M. Teng, S.S. Pan, C. Ye, G.H. Li, L.D. Zhang, Appl. Phys. Lett. 87 (2005) 231916.
[17] R.L. Thayer, C.A. Randall, S. Trolier-McKinstry, J. Appl. Phys. 94 (2003) 1941.
[18] N.M. Sammes, G.A. Tompsett, H. Nafe, F. Aldinger, J. Eur. Ceram. Soc. 19 (1999) 1801.
[19] A. Hameed, T. Montini, V. Gombac, P. Fornasiero, J. Am. Chem. Soc. 130 (2008) 9658.
[20] L. Li, Y.W. Yang, G.H. Li, L.D. Zhang, Small 2 (2006) 548.
[21] Y. Qiu, D. Liu, J. Yang, S. Yang, Adv. Mater. 18 (2006) 2604.
[22] T. Takeyama, N. Takahashi, T. Nakamura, S. Itoh, Solid State Commun. 133 (2005) 771.
[23] L. Zhou, W.Z. Wang, H.L. Xu, S.M. Sun, M. Shang, Chem. Eur. J. 15 (2009) 1776.
[24] C. Lin, D.Z. Tan, F.F. Luo, D.P. Chen, Q.Z. Zhao, J.R. Qiu, Z.Z. Xu, J. Alloys Compd. 507 (2010) L43.
[25] D. Louer, J.P. Auffredic, J.I. Langford, D. Ciosmak, J.C. Niepce, J. Appl. Crystallogr. 16 (1983) 183.
[26] V.K. Sankaranarayanan, N.S. Gajbhiye, Thermochim. Acta 153 (1989) 337.
[27] V.K. Sankaranarayanan, N.S. Gajbhiye, J. Am. Ceram. Soc. 73 (1990) 1301.
[28] J.I. Langford, A. Boultif, J.P. Auffredic, D. Louer, J. Appl. Crystallogr. 26 (1993) 22.
[29] N. Guillou, J.P. Auffredic, D. Louer, Powder Diffr. 10 (1995) 236.
[30] G. Fierro, S. Morpurgo, M. Lo Jacono, M. Inversi, I. Pettiti, Appl. Catal. A: Gen. 166 (1998) 407.
[31] E. Traversa, P. Nunziante, M. Sakamoto, Y. Sadaoka, M.C. Carotta, G. Martinelli, J. Mater. Res. 13 (1998) 1335.
[32] G.J. Zhang, Z.R. Shen, M. Liu, C.H. Guo, P.C. Sun, Z.Y. Yuan, B.H. Li, D.T. Ding, T.H. Chen, J. Phys. Chem. B 110 (2006) 25782.
[33] M. Liu, G.J. Zhang, Z.R. Shen, P.C. Sun, D.T. Ding, T.H. Chen, Solid State Sci. 11 (2008) 118.
[34] Z.R. Shen, G.J. Zhang, H.J. Zhou, P.C. Sun, B.H. Li, D.T. Ding, T.H. Chen, Adv. Mater. 20 (2008) 984.
[35] H.G. Zhang, Q.S. Zhu, Y. Wang, Chem. Mater. 17 (2005) 5824.
[36] Q.Y. Lu, F. Gao, S. Komarneni, J. Am. Chem. Soc. 126 (2004) 54.
[37] H.D. Yu, D.S. Wang, M.Y. Han, J. Am. Chem. Soc. 129 (2007) 2333.
[38] Z.F. Bian, J. Zhu, S.H. Wang, Y. Cao, X.F. Qian, H.X. Li, J. Phys. Chem. C 112 (2008) 6258.
[39] S.L. Mitchell, J. Guzman, Mater. Chem. Phys. 114 (2009) 462–466.
[40] S.F. Shao, G.J. Zhang, H.J. Zhou, P.C. Sun, Z.Y. Yuan, B.H. Li, D.T. Ding, T.H. Chen, Solid State Sci. 9 (2007) 725.
[41] O. Monnereau, L. Tortet, P. Llewellyn, F. Rouquerol, G. Vacquier, Solid State Ionics 157 (2003) 163.
[42] M. Rivenet, P. Roussel, F. Abraham, J. Solid State Chem. 181 (2008) 2586.
[43] S. Koutsopoulos, E. Dalas, Langmiur 17 (2001) 1074.
[44] Z.B. He, S.H. Yu, J.P. Zhu, Chem. Mater. 17 (2005) 2785.
[45] A.J. Xie, Y.H. Shen, C.Y. Zhang, Z.W. Yuan, X.M. Zhu, Y.M. Yang, J. Cryst. Growth 285 (2005) 436.
[46] H. Zheng, K.Y. Liu, H.Q. Cao, X.R. Zhang, J. Phys. Chem. C 113 (2009) 18259.
[47] L.S. Zhang, W.Z. Wang, J. Yang, Z.G. Chen, W.Q. Zhang, L. Zhou, S.W. Liu, Appl. Catal. A: Gen. 308 (2006) 105.
[48] T.P. Gujar, V.R. Shinde, C.D. Lokhande, R.S. Mane, S.H. Han, Appl. Surf. Sci. 250 (2005) 161.
[49] Y.S. Luo, S.Q. Li, Q.F. Ren, J.P. Liu, L.L. Xing, Y. Wang, Y. Yu, Z.J. Jia, J.L. Li, Cryst. Growth Des. 7 (2007) 87.
[50] J. Zhang, F.J. Shi, J. Lin, D.F. Chen, J.M. Gao, Z.X. Huang, X.X. Ding, C.C. Tang, Chem. Mater. 20 (2008) 2937.